Chemical Science

ROYAL SOCIETY OF CHEMISTRY

EDGE ARTICLE

View Article Online
View Journal | View Issue

Cite this: *Chem. Sci.*, 2026, **17**, 7699

All publication charges for this article have been paid for by the Royal Society of Chemistry

Diboron- and digermanium-doped dihydrodibenzohexacenes: Ge–B exchange to access boron-doped extended acenes

Heechan Kim, [a] Laura F. Peña,[bc] Adrian Espineira-Gutierrez, [bc] Carlos Romero-Nieto*[bc] and Robert J. Gilliard, Jr *[a]

Incorporation of main-group atoms into the backbone of polycyclic aromatic hydrocarbons offers an effective strategy to modulate their electronic structures. Boron and germanium doping is particularly attractive for enhancing optoelectronic and electrochemical properties. However, regioselective incorporation of these elements into extended π-conjugated systems remains limited due to synthetic challenges and stability issues. Herein, we report the synthesis of isomeric series of digermanium-(**2** and **6**) and diboron-(**4** and **8**) embedded dihydrodibenzohexacenes. The molecular structures of the four compounds were confirmed by single-crystal X-ray diffraction, revealing curved backbones for the digermanium-doped compounds **2** and **6**, whereas the diboron analogues **4** and **8** display a planar backbone incorporating two weakly antiaromatic C_5B rings. All compounds show efficient photoluminescence in both the solution- and solid-state, spanning the wide spectral regions from blue to orange. Electrochemical studies of **4** and **8** reveal two quasi-reversible reduction processes, with the pseudo-*para* diboron-substituted isomer **8** exhibiting slightly anodically shifted reduction potentials. These results demonstrate that diboron and digermanium doping provides a promising platform for the development of stable, emissive, and redox-active polycyclic aromatic hydrocarbons.

Received 19th December 2025
Accepted 13th February 2026

DOI: 10.1039/d5sc09987k

rsc.li/chemical-science

Introduction

A powerful strategy for modulating the electronic structures of extended polycyclic aromatic hydrocarbons (PAHs) is the incorporation of electropositive main-group elements, such as boron and germanium, into the π-backbone.[1–3] This substitution profoundly alters the energies and distributions of the frontier molecular orbitals (FMOs), thereby reshaping the optical, redox, and chemical characteristics of the PAH framework. Tricoordinate boron, with its vacant p_z orbital, engages in π* interactions with the conjugated system, lowering the lowest unoccupied molecular orbital (LUMO) energy and imparting distinctive luminescent, Lewis acidic, and redox-active properties.[4–13] Tetracoordinate germanium atoms not only suppress molecular vibrations, but also provide a heavy-atom effect that could enhance radiative decay, resulting in enhanced quantum yields and photostability.[14,15] These attributes render B and Ge-doped, extended PAHs highly promising for applications in room-temperature phosphorescence,[16–18] organic light-emitting diodes (OLEDs),[19–22] organic field-effect transistors (OFETs),[23–25] and stimuli-responsive materials.[26–29]

Selected examples of extended PAHs doped with multiple Ge atoms (Fig. 1A) include the trigermasumanene (**I**),[30] synthesized *via* threefold Rh-catalyzed cyclodehydrogenation, which stands as a rare case of a polycyclic scaffold incorporating three germanium centers. Our laboratory reported pyrene-fused bis(N-heterocyclic germylenes).[31] Despite these advances, linearly extended PAHs incorporating multiple germanium remain scarce with Yoshikai's report on a ladder-type digermaindenofluorene (**II**)[32] as the sole example, largely due to the limited availability of reliable synthetic methods for site-specific germanium incorporation. There are several reports on linearly fused, diboron-doped PAHs (Fig. 1B). The tetrel–boron exchange reactions are central to access these diboraacenes; for example, heating of 1,2-bis(trimethylsilyl) benzene with BBr_3 yields a diboradihydroanthracene framework (**III**) in which a six-membered B_2C_4 ring is formed *via* self-assembly.[33–37] This methodology was subsequently extended to produce diboron-doped pentacene (**IV**),[38] heptacene (**V**),[39] and nonacene (**VI**)[39] congeners by Ashe and Wang. Our laboratory reported a diboratapentacene dianion (**VII**),[40] where the tetrahydrodiborapentacene backbone was prepared *via* a Si–B exchange reaction from a tetrahydrodisilapentacene precursor.

Herein, we report the synthesis and characterization of isomeric digermadihydrodibenzohexacenes (**2** and **6**) and

[a]*Department of Chemistry, Massachusetts Institute of Technology, Cambridge, Massachusetts 02139-4307, USA. E-mail: gilliard@mit.edu*

[b]*Faculty of Pharmacy, University of Castilla-La Mancha, Calle Almansa 14 – Edif. Bioincubadora, 02008, Albacete, Spain. E-mail: carlos.romeronieto@uclm.es*

[c]*Instituto Regional de Investigación Científica Aplicada (IRICA), University of Castilla–La Mancha, 13071 Ciudad Real, Spain*

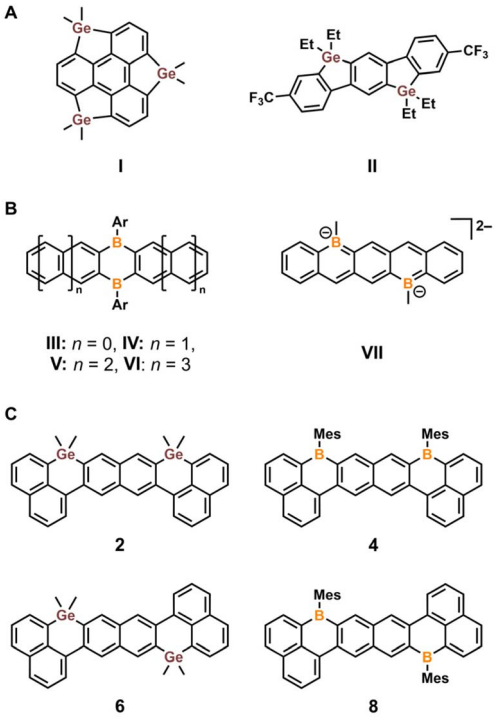

Fig. 1 Chemical structures of (A) PAHs with multiple germanium doping: trigermasumanene (I) and digermaindenofluorene (II) and (B) diboron-incorporated dihydroacenes (III–VI) with two boron atoms located in the same ring and diboratapentacene dianion (VII) with two boron atoms located in different rings. (C) This work reporting digermanium- and diboron-doped dihydrodibenzohexacenes.

diboradihydrodibenzohexacenes (**4** and **8**) (Fig. 1C). The digermanium-doped **2** and **6** are isolated as crystalline, air- and moisture-stable solids, expanding the scope of Group 14 element-doped PAHs. Treatment of **2** and **6** with BBr_3, and quenching with MesMgBr afforded **4** and **8**, demonstrating Ge–B exchange as an effective strategy to access boron-doped heterocycles. Compounds **2** and **6** display bright deep-blue emission in solution, while extended conjugation through the tricoordinate boron centers shifts the emission to green (**4**) and yellow (**8**) compared to the digermanium congeners. Additionally, the diboron-doped **4** and **8** display stepwise two-electron electrochemical reductions. Collectively, these results highlight this new family of linearly extended digermanium- and diboron-doped PAHs as multicolor-emissive and redox-active materials.

Results and discussion

Syntheses of isomeric digermanium- and diboron-doped dihydrodibenzoacenes

Treatment of *syn*- and *anti*-tetrabromoternaphthalene (**1** and **5**, respectively)[41] with excess *tert*-butyllithium generated the corresponding tetralithiated intermediates *in situ* (Scheme 1). Subsequent quenching with dimethylgermanium dichloride (Me_2GeCl_2) afforded the desired digermacyclic compounds **2** and **6** as off-white solids in 92% and 81% yields, respectively. Both **2** and **6** are remarkably stable toward air and moisture and even withstand purification by silica-gel chromatography. Despite the curved molecular geometries (*vide infra*), the NMR spectra of **2** and **6** indicate that the molecular curvature is conformationally flexible and dynamically averaged in solution. They exhibit moderate solubility (>20 mg mL^{-1}) in common organic solvents (CH_2Cl_2, $CHCl_3$, toluene, THF, and EtOAc), likely due to their bent molecular framework, which suppresses intermolecular π–π stacking.

Exposure of solid **2** and **6** to neat BBr_3 immediately produced a deep-red homogeneous solution, which rapidly yielded dark-orange precipitates of **3** and **7**, respectively. These highly moisture-sensitive, Lewis-acidic intermediates are poorly soluble in all common organic solvents and were therefore converted into **4** and **8** (without isolation) by treatment with MesMgBr. Compounds **4** and **8** were obtained as yellow and orange solids in 64% and 67% two-step yields, respectively. Similar to their germanium precursors, both **4** and **8** exhibit excellent air and moisture stability, allowing for purification by column chromatography. The ^{11}B NMR spectra of **4** and **8** each display a broad resonance near $\delta = 65$ ppm, consistent with the presence of tricoordinate boron centers. The ^{1}H NMR resonances for the protons in the central naphthalene rings of **4** and **8** are downfield shifted (9.41 and 8.47 ppm for **4**; 9.28 and 8.68 ppm for **8**) compared to those of **2** and **6** (8.61 and 8.18 ppm for **2**; 8.56 and 8.25 ppm for **6**), indicating the electron-withdrawing nature of the tricoordinate boron centers.

It is noteworthy that all attempts to access **4** or **8** *via* the corresponding disilacyclic or distannacyclic precursors were unsuccessful. The previously reported disilacycle[42] proved unreactive toward Si–B exchange with BBr_3, failing to afford the intermediate **3** (Scheme S5). Efforts to prepare and isolate the analogous distannacycle were also unsuccessful, likely due to the poor hydrolytic stability of the Sn–C bonds (Scheme S6).[43] These observations highlight intrinsic trade-offs that hinder tetrel–boron exchange reactions: silacycles are chemically robust but require significant activation energy to undergo Si–B exchange,[6,44] whereas stannacycles possess the required reactivity but sometimes lack sufficient stability for isolation. These limitations become especially pronounced in systems with extended conjugation or multiple boron centers where solubility and regioselectivity issues further complicate synthesis. The digermacyclic scaffolds (**2** and **6**) represent an effective balance between reactivity and stability, as discussed in the following section.

Mechanism of the tetrel–boron exchange reactions

To gain deeper insight into the mechanistic differences among Si–B, Ge–B, and Sn–B exchange reactions, we performed *ab initio* calculations at the B3LYP-D3(BJ)/def2-SVP level of theory using the CPCM solvation model for BBr_3 ($\varepsilon = 2.58$). To simplify the reaction of ditetrel-substituted dihydrodibenzohexacenes (*e.g.*, **2** and **6**) with BBr_3 to generate the diboron-doped dihydrodibenzohexacenes (**4** and **8**), the parent structure was truncated to a model system (**SM**), in which the Group 14 element bridges a naphthalene and a phenyl ring of the 1-

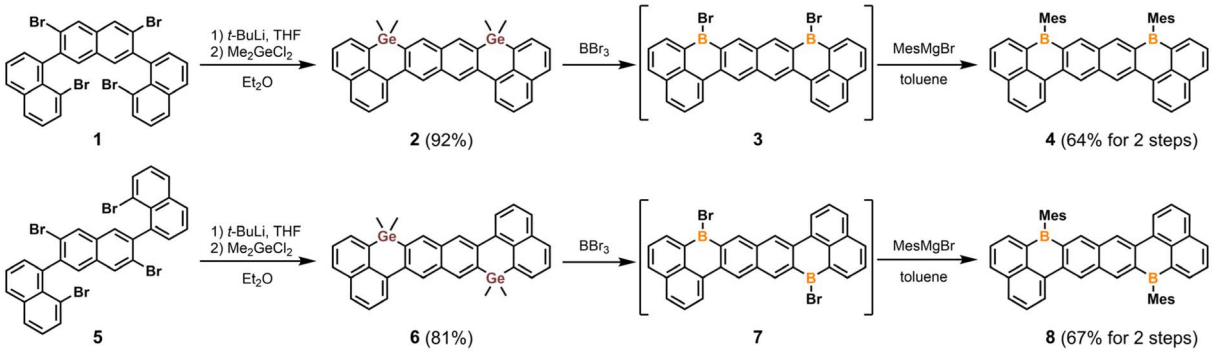

Scheme 1 Syntheses of digermanium- and diboron-doped dihydrodibenzoacenes **2**, **4**, **6**, and **8**.

phenylnaphthalene scaffold (Fig. 2). This model allows analysis of a single tetrel–boron exchange reaction with BBr_3. The optimized structures and relative Gibbs free energies (ΔG) of all relevant stationary points are summarized in the corresponding potential energy surface (PES) shown in Fig. 2.

The tetrel–boron exchange reaction of **SM** proceeds in a manner analogous to that reported for the reaction between dibenzosilole and BBr_3.[44] Initial association of **SM** with BBr_3 forms the encounter complex **Int1** *via* a shallow transition state **TS1**. Subsequent conversion of **Int1** to the ring-opened intermediate **Int2** occurs through **TS2**, which involves concerted B–Br bond cleavage and E–Br bond formation. Owing to the significant distortion of the tetrel-containing six-membered ring in both **Int1** and **TS2**, coordination of BBr_3 preferentially occurs at the phenyl ring rather than the naphthalene ring (for detailed information see Fig. S24). A second tetrel–boron exchange then proceeds through **Int3** to afford the boracycle (**Product**), accompanied by release of Me_2ECl_2 as a byproduct. Overall, the reaction is highly exothermic, with calculated reaction free energies of −147.6 kJ mol^{-1} for Si, −172.1 kJ mol^{-1} for Ge, and −255.9 kJ mol^{-1} for Sn.

These DFT analyses reveal pronounced differences in the reactivity of tetrel heterocycles toward BBr_3. For the Si and Ge systems, the rate-determining step (RDS) corresponds to **TS2**, whereas for Sn the highest barrier is associated with **TS1**. The calculated activation free energies are 110.6 kJ mol^{-1} for Si, 83.4 kJ mol^{-1} for Ge, and 41.9 kJ mol^{-1} for Sn. These trends indicate that Si–B exchange is kinetically inaccessible at room temperature, while Ge–B and Sn–B exchange reactions are feasible under mild conditions. Taken together, these results highlight germacyclic scaffolds as an optimal balance between stability and reactivity. The Ge–C bonds provide sufficient hydrolytic robustness while maintaining adequate reactivity to enable facile Ge–B exchange with BBr_3 at room temperature, offering a practical and generalizable strategy for the synthesis of boron-doped acenes.

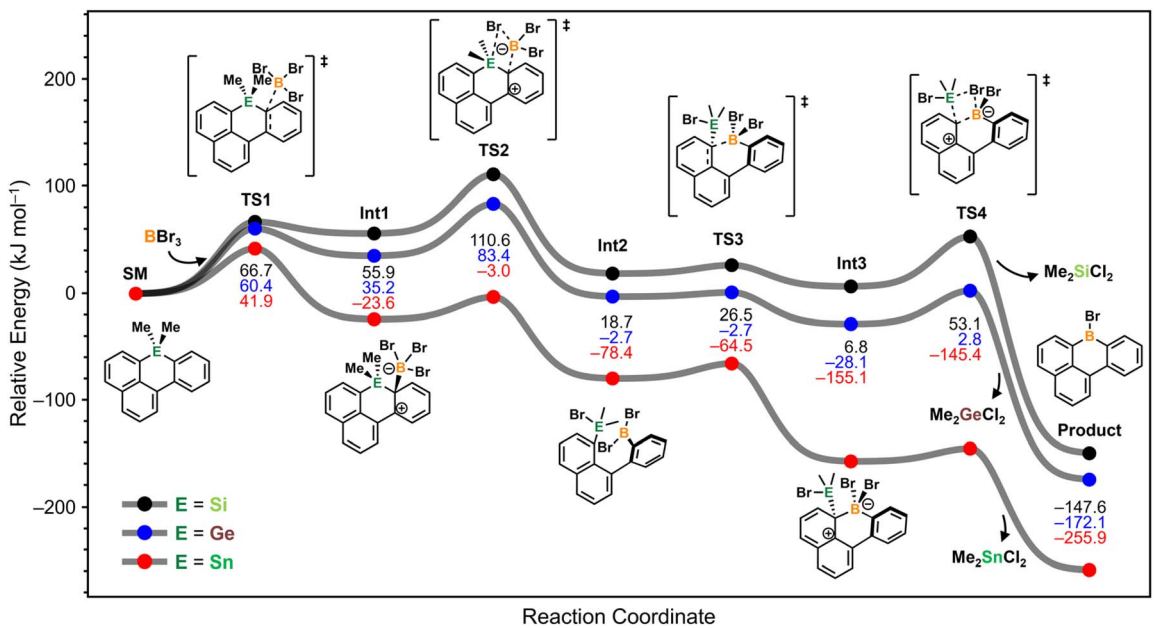

Fig. 2 Calculated mechanism for the tetrel–B exchange reaction from **SM** to **Product**. The geometries were optimized at the B3LYP-D3(BJ)/def2-SVP (CPCM, BBr_3) level of theory.

Single crystal X-ray diffraction studies

Single-crystal X-ray diffraction (SC-XRD) analyses unambiguously confirmed the molecular structures of **2**, **4**, **6**, and **8** (Fig. 3). The six-membered germacyclic rings in both the *syn*- (**2**) and *anti*- (**6**) digermadibenzohexacenes deviate notably from ideal hexagonal geometry (Fig. 3A and C), exhibiting Ge–C bond lengths in the range of 1.924(4)–1.938(4) Å and small C–Ge–C bond angles (100.85(7)–101.63(6)°), consistent with the limited sp^3 hybridization at the germanium centers. These structural features impart a pronounced bending to the molecular framework, which arises primarily from steric repulsion between hydrogen atoms at the bay regions. The torsion angles at the bay regions are 22.9(5)° for **2**, and 16.7(2)° and 20.3(2)° for **6**, respectively. The intramolecular Ge···Ge distances are 8.2265(8) Å for **2** and 8.8640(6) Å for **6**. As demonstrated by their herringbone packing motifs (Fig. S11 and S13), compound **2** exhibits a solid-state packing arrangement that is completely free of face-to-face π–π stacking, and **6** shows only minimal intermolecular π–π interactions between peripheral naphthalene units. Indeed, the curved molecular geometries of **2** and **6** account for their moderate solubility in common organic solvents.

In stark contrast, the corresponding diboron analogues **4** and **8** adopt essentially planar geometries (Fig. 3B and D), with the pendent mesityl groups oriented nearly perpendicular to the π-conjugated backbone. The B···B distances are 7.525(8) Å for **4** and 8.149(2) Å for **8**. Within the planar six-membered boracyclic rings, the C–B bond lengths range from 1.535(9) to 1.556(2) Å, which are slightly shorter than those in triphenylborane (1.570–1.588 Å).[45] These observations are consistent with enhanced π-delocalization across the boron-containing framework. Compound **4** adopts a slipped, head-to-tail π-dimeric packing motif with the shortest centroid-to-centroid distance of 3.323(4) Å (Fig. S12). Compound **8**, by contrast, crystallizes with two toluene molecules per formula unit, and the perpendicular mesityl substituents at each boron center effectively prevent close π–π contacts in the solid-state (Fig. S14).

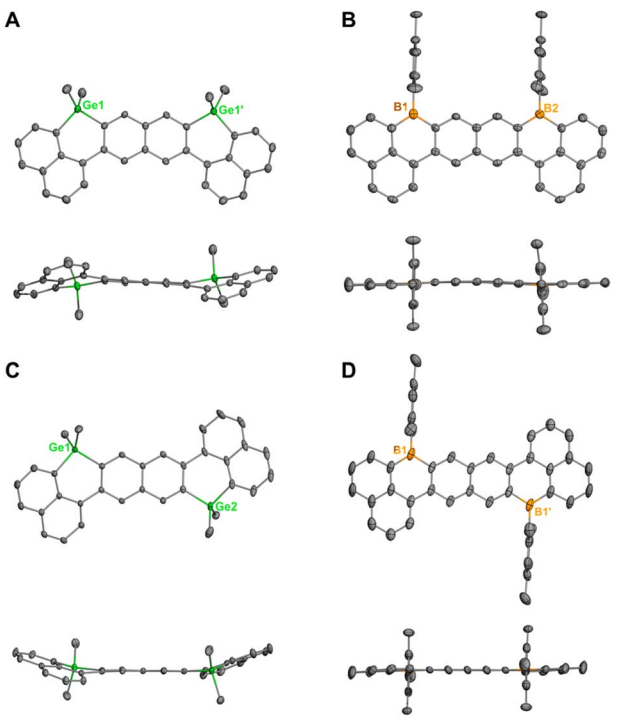

Fig. 3 X-ray structures of **2** (A), **4** (B), **6** (C), and **8** (D). Thermal ellipsoids were drawn at 50% probability level. Solvent molecules and hydrogen atoms were omitted for clarity.

Electronic structures

To elucidate the influence of germanium *versus* boron substitution on the electronic structures, density functional theory (DFT) calculations were performed at the B3LYP-D3(BJ)/def2-TZVP//B3LYP-D3(BJ)/def2-SVP level with CH_2Cl_2 as solvent using the conductor-like polarizable continuum model (CPCM). The calculated FMOs and energy levels are summarized in Fig. 4 and S25–S28. In all four compounds, the FMOs are predominantly composed of delocalized π-orbitals spanning the three naphthalene units.

In the digermanium-doped **2** and **6**, the germanium atoms show negligible contribution to the π-manifold, confirming their electronically isolated nature. In contrast, the boron centers in **4** and **8** exhibit substantial orbital coefficients in the LUMOs, indicating active participation in the conjugated framework. Consequently, the LUMO energies of **4** (−2.57 eV) and **8** (−2.64 eV) are significantly lower than those of **2** (−1.83 eV) and **6** (−1.98 eV). Because Ge to B substitution has minimal effect on the HOMO energies, the pronounced stabilization of the LUMO levels directly accounts for the narrower HOMO–LUMO gaps observed in **4** and **8**.

The aromaticity of the planar **4** and **8** was assessed by two-dimensional nucleus-independent chemical shift (2D-NICS) calculations, which were performed at the B3LYP-D3(BJ)/def2-SVP level of theory (Fig. S29). The $NICS(1)_{zz}$ values at the centers of the C_6 rings within the naphthalene units range from −26 ppm to −21 ppm, characteristic of aromatic systems. In contrast, the corresponding values for the six-membered boracyclic rings lie between +4 and +10 ppm, indicative of weak antiaromaticity. This trend is consistent with the reported antiaromatic character of dihydrodiboraacene derivatives **III**–**VI**.[39]

Photophysical properties

To investigate the structure-dependent optoelectronic properties, the absorption and emission spectra of **2**, **4**, **6**, and **8** were measured in both CH_2Cl_2 solution and solid state (Fig. 5 and Table 1). Compounds **2**, **4**, **6**, and **8** exhibit characteristic absorption spectra with large molar absorptivity exceeding 30 000 M^{-1} cm^{-1} at their absorption maxima. The germacycles **2** and **6** display absorption maxima at λ_{abs} = 370 and 381 nm, whereas the boracycles **4** and **8** exhibit markedly red-shifted absorptions at λ_{abs} = 473 and 502 nm, respectively. Because the tetracoordinate germanium centers are electronically isolated from the π-conjugated framework, the observed

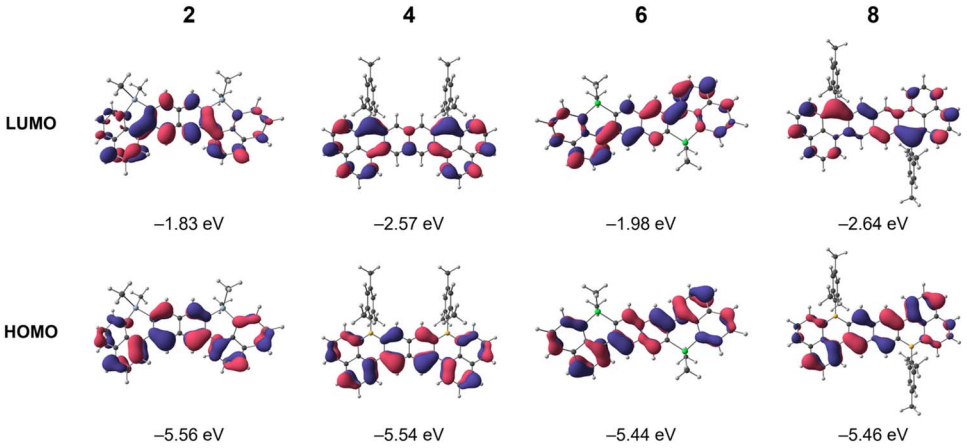

Fig. 4 Frontier molecular orbitals of **2**, **4**, **6**, and **8** calculated at the B3LYP-D3(BJ)/def2-TZVP (CPCM, CH_2Cl_2)//B3LYP-D3(BJ)/def2-SVP (CPCM, CH_2Cl_2) level of theory.

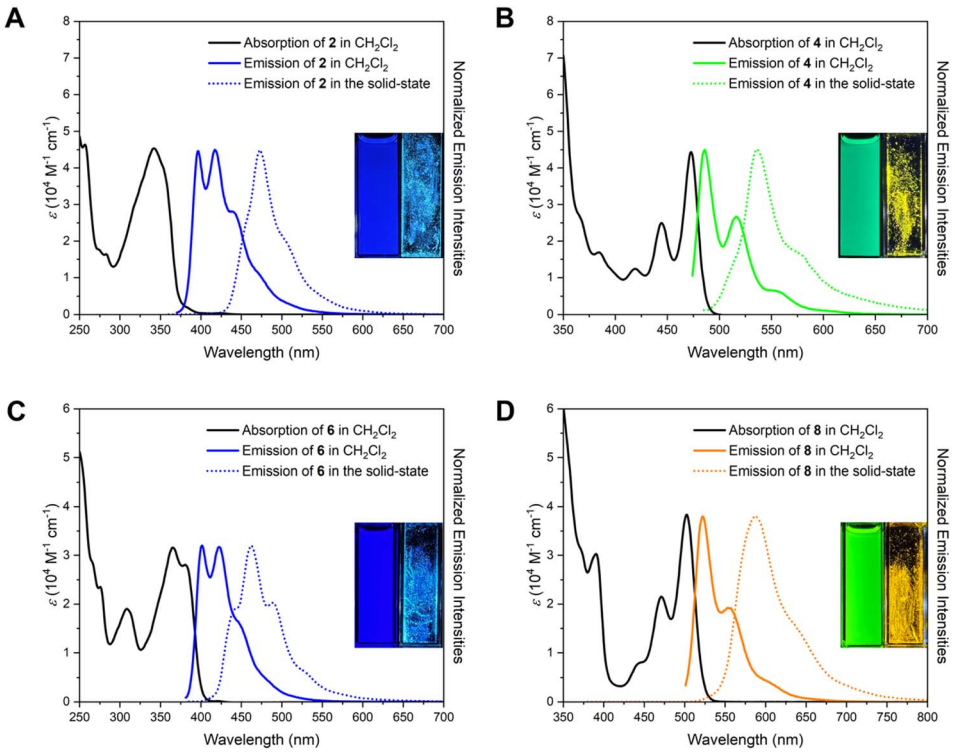

Fig. 5 Solution-state absorption (black lines, 10 mM in CH_2Cl_2), solution-state emission (colored solid lines, in CH_2Cl_2), and solid-state emission (colored dotted lines) spectra of **2** (A), **4** (B), **6** (C), and **8** (D). The insets show images of each sample in solution- and solid-state under 365 nm irradiation.

bathochromic shift upon boron incorporation reflects the extended π-delocalization mediated by the tricoordinate boron atoms.

Time-dependent DFT (TD-DFT) calculations (TD-B3LYP-D3(BJ)/def2-TZVP (CPCM, CH_2Cl_2)//B3LYP-D3(BJ)/def2-SVP (CPCM, CH_2Cl_2)) further clarify these electronic transitions. Compounds **4**, **6**, and **8** exhibit $S_0 \rightarrow S_1$ transitions with predominant (>95%) HOMO → LUMO character and large oscillator strengths ($f > 0.5$) (Tables S6–S8). In contrast, compound **2** shows an $S_0 \rightarrow S_1$ transition composed of mixed HOMO → LUMO + 1 (60%), HOMO − 1 → LUMO + 2 (2%), HOMO − 1 → LUMO (33%) and HOMO − 2 → LUMO + 1 (2%) transitions, accompanied by a very small oscillator strength ($f = 0.048$) (Table S5). This unusually weak S_1 transition originates from destructive interference between HOMO → LUMO + 1 and HOMO − 1 → LUMO configurations, leading to configuration–interaction cancellation of the transition dipole moment. It explains the weak absorption tail around 380 nm with a low molar absorptivity ($\varepsilon < 2000\ M^{-1}\ cm^{-1}$), consistent with the calculated absorption spectrum of **2** (Fig. S30). The observed

Table 1 Summary of the photophysical properties of **2**, **4**, **6**, and **8**

	λ_{abs}[a] (nm)	ε[b] (M^{-1} cm^{-1})	λ_{em}[c] (nm)	λ_{em}[d] (nm)	Stokes shift (cm^{-1})	Φ_F[e]	Φ_F[f]	τ[g] (ns)	k_r (10^7 s^{-1})	k_{nr} (10^7 s^{-1})
2	370	45 300	417	473	2400	0.14	0.47	11.7	1.2	7.5
4	473	44 000	486	536	566	0.67	0.14	5.6	12	5.9
6	381	31 600	401	462	1310	0.54	0.21	1.8	30	2.6
8	502	38 300	522	588	763	0.40	0.15	7.2	5.6	8.4

[a] The longest experimental absorption maximum wavelengths in CH_2Cl_2. [b] Extinction coefficient at the longest absorption maximum wavelengths in CH_2Cl_2. [c] Emission maximum in CH_2Cl_2. [d] Emission maximum in the solid-state. [e] Absolute fluorescence quantum yields in CH_2Cl_2 determined by a calibrated integrating sphere system. [f] Absolute fluorescence quantum yields in the solid-state determined by a calibrated integrating sphere system. [g] Fluorescence lifetimes in CH_2Cl_2 determined by time-correlated single photon counting (TCSPC) measurements.

intense band at 370 nm corresponds instead to the S_3 transition ($f = 1.40$).

The CH_2Cl_2 solution samples of **4**, **6**, and **8** show emissions that mirror their absorption profiles, with $\lambda_{em} = 486$, 401, and 522 nm, respectively. Compound **2**, however, deviates from the mirror-image relationship, displaying an emission maximum at $\lambda_{em} = 417$ nm. This anomaly is attributed to the aforementioned mixing between the S_1 and S_3 states. Nonetheless, vibrational fine structures are evident in all emission spectra. The fluorescence quantum yields (Φ_F) in CH_2Cl_2 are moderate to high: 0.14 for **2**, 0.67 for **4**, 0.54 for **6**, and 0.40 for **8**.

In the solid-state, all four compounds exhibit red-shifted emissions with λ_{em} values of 473 nm (**2**), 536 nm (**4**), 462 nm (**6**), and 588 nm (**8**). Notably, compound **2** shows an enhanced fluorescence quantum yield ($\Phi_F = 0.47$) in the solid-state compared to its solution value ($\Phi_F = 0.14$). This aggregation-induced emission enhancement (AIEE) observed for **2** is attributed to the restriction of intramolecular motions (RIM), together with the absence of face-to-face π–π stacking in the solid-state packing structure (Fig. S11; *vide supra*). In contrast, the solid-state quantum yields of **4**, **6**, and **8** are lower than their solution-state counterparts, which we attribute to intermolecular π–π stacking interactions that facilitate exciton coupling between neighboring molecules. The reduction in Φ_F is more pronounced for **4** (0.67 → 0.14) than for **6** (0.54 → 0.21) and **8** (0.40 → 0.15), consistent with its significant π–π stacking interactions (Fig. S12–14).

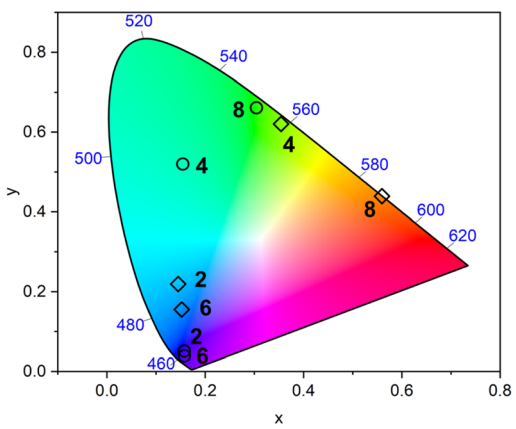

Fig. 6 Chromaticity coordinates (CIE) of **2**, **4**, **6**, and **8** in CH_2Cl_2 (black circles) and in the solid-state (black squares).

Compound **8** exhibits long-wavelength solid-state emission tails extending beyond 700 nm. This behavior is noteworthy and comparable to that of boron-doped polycyclic aromatic hydrocarbons with significantly more extended π-conjugation, including diboron-doped dihydroheptacene (**V**),[39] dihydrononacene (**VI**),[39] and tetraboron-doped tetrahydrononacene,[26] underscoring the effectiveness of regioselective boron incorporation in **8**. The structure- and phase-dependent emission properties of **2**, **4**, **6**, and **8** are highlighted in the chromaticity coordinates (Fig. 6).

Electrochemistry

The boraacenes **4** and **8** exhibit quasi-reversible two-electron reduction processes, as revealed by cyclic voltammetry (CV) (Fig. 7 and S20–S23). Differential pulse voltammetry (DPV) measurements show two well-resolved redox couples with half-

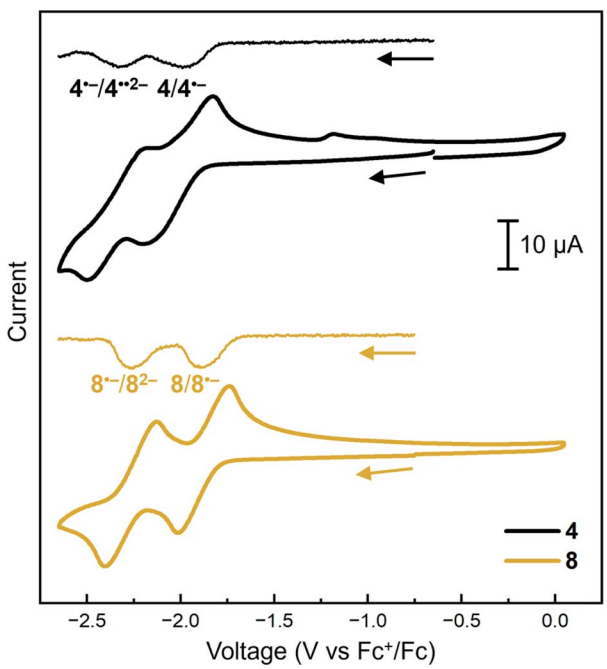

Fig. 7 Cyclic voltammetry and differential pulse voltammetry of **4** (black lines) and **8** (brown lines) in THF with *n*-Bu_4PF_6 (0.2 M) as the supporting electrolyte. Scan rate = 100 mV s^{-1}. Sample concentration = 2 mM.

wave potentials ($E_{1/2}$) of −1.99 and −2.33 V *vs.* Fc^+/Fc for **4**, and −1.89 and −2.28 V *vs.* Fc^+/Fc for **8**. These reduction potentials are slightly less negative than those reported for diboradihydroheptacene (−2.05 and −2.69 V *vs.* Fc^+/Fc), likely reflecting the weaker electron-donating ability of the naphthalene units in **4** and **8** relative to the anthracene skeleton in the heptacene analogue (**IV**).[39] Notably, compound **8** displays uniformly higher (less negative) reduction potentials than **4**, consistent with stronger electronic communication between the two boron centers located at the pseudo-*para* positions across the extended π-conjugated backbone. This enhanced delocalization renders the scaffold more electron-deficient, thereby stabilizing the reduced states and shifting the redox potentials anodically.

Conclusions

The digermanium- (**2** and **6**) and diboron- (**4** and **8**) doped dihydrodibenzohexacenes were synthesized and fully characterized using multinuclear NMR spectroscopy and single-crystal X-ray diffraction. Compounds **2** and **6** adopt curved geometries as a result of steric strain imposed by the two bulky C_5Ge rings, whereas the diboron analogues **4** and **8** exhibit planar frameworks that promote extended π-conjugation through effective overlap with the empty p_z orbitals of the tricoordinate boron centers. Such structural differences are directly reflected in their photophysical behavior, with the digermanium-doped derivatives displaying blue emission, while the diboron-doped compounds show pronounced bathochromic shifts leading to green to orange emission. Electrochemical studies of **4** and **8** reveal two quasi-reversible reduction processes, further highlighting their potential as redox-active π-conjugated materials. Collectively, these results expand the synthetic and structural landscape of heteroatom-doped PAHs and underscore the utility of main-group element incorporation for the development of functional organic materials.

Author contributions

H. Kim: conceptualization, formal analysis, investigation, methodology, visualization, writing – original draft, writing – review & editing. L. F. Peña and A. Espineira-Gutierrez: conceptualization, formal analysis, investigation, methodology. C. Romero-Nieto: conceptualization, funding acquisition, project administration, supervision, validation, writing – review & editing. R. J. Gilliard: conceptualization, funding acquisition, project administration, supervision, validation, writing – original draft, writing – review & editing.

Conflicts of interest

There are no conflicts to declare.

Data availability

Supplementary information (SI): including experimental details, NMR spectra, absorption spectra, emission spectra, electrochemical data, single-crystal X-ray diffraction data, and computational details. See DOI: https://doi.org/10.1039/d5sc09987k.

CCDC 2499454 (**2**), 2499455 (**4**), 2499456 (**6**) and 2499457 (**8**) contain the supplementary crystallographic data for this paper.[46a–d]

Acknowledgements

We are grateful to the Arnold and Mabel Beckman Foundation for support of this work. We acknowledge the National Research Foundation (NRF) of Korea for a postdoctoral fellowship for H. Kim (RS-2024-00407978). C. R. N. thanks the ERC for the Consolidator grant (ref. 101087685). Projects PID2021-125794OB-I00 and CNS2022-136028 funded by MICIU/AEI/10.13039/501100011033; PRTR-C17.I1 funded by MCIN with funding from the European Union NextGenerationEU and the JCCM; and SBPLY/21/180501/000185 and SBPLY/21/180501/000185 funded by JCCM and "ERDF A way to make Europe" are gratefully acknowledged.

Notes and references

1 X.-Y. Wang, X. Yao, A. Narita and K. Müllen, *Acc. Chem. Res.*, 2019, **52**, 2491–2505.
2 A. Borissov, Y. K. Maurya, L. Moshniaha, W.-S. Wong, M. Żyła-Karwowska and M. Stępień, *Chem. Rev.*, 2022, **122**, 565–788.
3 A.-L. Thömmes and D. Scheschkewitz, *Angew. Chem., Int. Ed.*, 2026, **65**, e14344.
4 C.-L. Deng, A. D. Obi, B. Y. E. Tra, S. K. Sarkar, D. A. Dickie and R. J. Gilliard, *Nat. Chem.*, 2024, **16**, 437–445.
5 K. K. Hollister, A. Molino, V. V. Le, N. Jones, W. J. Smith, P. Müller, D. A. Dickie, D. J. D. Wilson and R. J. Gilliard, *Chem. Sci.*, 2024, **15**, 14358–14370.
6 H. Kim and R. J. Gilliard Jr, *J. Am. Chem. Soc.*, 2025, **147**, 23213–23225.
7 N. C. Frey, K. K. Hollister, C. C. Taylor, N. Jones, D. A. Dickie and R. J. Gilliard, *J. Mater. Chem. C*, 2025, **13**, 19778–19787.
8 K. K. Hollister, A. Molino, G. Breiner, J. E. Walley, K. E. Wentz, A. M. Conley, D. A. Dickie, D. J. D. Wilson and R. J. Gilliard Jr, *J. Am. Chem. Soc.*, 2022, **144**, 590–598.
9 T. Kushida, S. Shirai, N. Ando, T. Okamoto, H. Ishii, H. Matsui, M. Yamagishi, T. Uemura, J. Tsurumi, S. Watanabe, J. Takeya and S. Yamaguchi, *J. Am. Chem. Soc.*, 2017, **139**, 14336–14339.
10 J. M. Farrell, C. Mützel, D. Bialas, M. Rudolf, K. Menekse, A.-M. Krause, M. Stolte and F. Würthner, *J. Am. Chem. Soc.*, 2019, **141**, 9096–9104.
11 R. R. Maar, B. D. Katzman, P. D. Boyle, V. N. Staroverov and J. B. Gilroy, *Angew. Chem., Int. Ed.*, 2021, **60**, 5152–5156.
12 J.-J. Zhang, L. Yang, F. Liu, Y. Fu, J. Liu, A. A. Popov, J. Ma and X. Feng, *Angew. Chem., Int. Ed.*, 2021, **60**, 25695–25700.
13 Y. Yu, C. Wang, F.-F. Hung, L. Jiang, C.-M. Che and J. Liu, *Angew. Chem., Int. Ed.*, 2025, **64**, e202501645.
14 T. Delouche, M. Hissler and P.-A. Bouit, *Coord. Chem. Rev.*, 2022, **464**, 214553.

15 J. Li, Q. Xia, J. Li, X. Yu, Z. Feng, Y. Zhang, T. Wu, Z. Xu, H. Lin and J. Qian, *Aggregate*, 2025, **6**, e70148.
16 J. Liu, J. Yao, R. Mu, X. Mao, H. Li, J. Sun, J. Huang, Q. Feng, X. Cao, J. Wang and H. Huang, *Angew. Chem., Int. Ed.*, 2025, **64**, e202509104.
17 Q. Feng, J. Yao, Q. Wu, Y. Qiu, Z. Wang, X. Wang, W. Chen, S. Tong, X. Cao, J. Sun, Q. Ye, J. Liu, D. Wang, J. Wang and H. Huang, *Chem. Sci.*, 2025, **16**, 17470–17479.
18 A. E. R. Watson, S. Y. Tao, A. Siemiarczuk, P. D. Boyle, P. J. Ragogna and J. B. Gilroy, *Angew. Chem., Int. Ed.*, 2025, **64**, e202414534.
19 A. John, M. Bolte, H.-W. Lerner, G. Meng, S. Wang, T. Peng and M. Wagner, *J. Mater. Chem. C*, 2018, **6**, 10881–10887.
20 G. Li, K. Xu, J. Zheng, X. Fang, Y.-F. Yang, W. Lou, Q. Chu, J. Dai, Q. Chen, Y. Yang and Y.-B. She, *Nat. Commun.*, 2023, **14**, 7089.
21 X. Tian, Z. Fan, Z. Li, S. Zhang, Z. Li, X. Zhuang, Y. Wang and C. Dou, *Angew. Chem., Int. Ed.*, 2025, **64**, e202500110.
22 G. Meng, L. Liu, Z. He, D. Hall, X. Wang, T. Peng, X. Yin, P. Chen, D. Beljonne, Y. Olivier, E. Zysman-Colman, N. Wang and S. Wang, *Chem. Sci.*, 2022, **13**, 1665–1674.
23 S. K. Mellerup and S. Wang, *Trends Chem.*, 2019, **1**, 77–89.
24 W. Sun, J. Guo, Z. Fan, L. Yuan, K. Ye, C. Dou and Y. Wang, *Angew. Chem., Int. Ed.*, 2022, **61**, e202209271.
25 K. Zhao, Z.-F. Yao, Z.-Y. Wang, J.-C. Zeng, L. Ding, M. Xiong, J.-Y. Wang and J. Pei, *J. Am. Chem. Soc.*, 2022, **144**, 3091–3098.
26 C. Chen, Y. Guo, Z. Chang, K. Müllen and X.-Y. Wang, *Nat. Commun.*, 2024, **15**, 8555.
27 S. K. Mellerup and S. Wang, *Chem. Soc. Rev.*, 2019, **48**, 3537–3549.
28 N. Ando, T. Yamada, H. Narita, N. N. Oehlmann, M. Wagner and S. Yamaguchi, *J. Am. Chem. Soc.*, 2021, **143**, 9944–9951.
29 P. Li, D. Shimoyama, N. Zhang, Y. Jia, G. Hu, C. Li, X. Yin, N. Wang, F. Jäkle and P. Chen, *Angew. Chem., Int. Ed.*, 2022, **61**, e202200612.
30 D. Zhou, Y. Gao, B. Liu, Q. Tan and B. Xu, *Org. Lett.*, 2017, **19**, 4628–4631.
31 K. E. Krantz, S. L. Weisflog, W. Yang, D. A. Dickie, N. C. Frey, C. E. Webster and R. J. Gilliard, *Chem. Commun.*, 2019, **55**, 14954–14957.
32 B. Wu and N. Yoshikai, *Angew. Chem., Int. Ed.*, 2015, **54**, 8736–8739.
33 C. Reus, S. Weidlich, M. Bolte, H.-W. Lerner and M. Wagner, *J. Am. Chem. Soc.*, 2013, **135**, 12892–12907.
34 A. John, M. Bolte, H.-W. Lerner and M. Wagner, *Angew. Chem., Int. Ed.*, 2017, **56**, 5588–5592.
35 Y.-K. Chen, J. Lei, P.-C. Liu, C.-H. Lin, Y.-M. Chen, W.-S. Chang, I. C. Chen, L.-Y. Hsu and T.-L. Wu, *J. Am. Chem. Soc.*, 2025, **147**, 45603–45617.
36 C. Saalfrank, F. Fantuzzi, T. Kupfer, B. Ritschel, K. Hammond, I. Krummenacher, R. Bertermann, R. Wirthensohn, M. Finze, P. Schmid, V. Engel, B. Engels and H. Braunschweig, *Angew. Chem., Int. Ed.*, 2020, **59**, 19338–19343.
37 Y.-K. Chen, J. Lei, P.-C. Liu, C.-H. Lin, Y.-M. Chen, W.-S. Chang, I. C. Chen, L.-Y. Hsu and T.-L. Wu, *J. Am. Chem. Soc.*, 2025, **147**, 45603–45617.
38 J. Chen, J. W. Kampf and A. J. Ashe III, *Organometallics*, 2008, **27**, 3639–3641.
39 C. Chen, M.-W. Wang, X.-Y. Zhao, S. Yang, X.-Y. Chen and X.-Y. Wang, *Angew. Chem., Int. Ed.*, 2022, **61**, e202200779.
40 J. E. Barker, A. D. Obi, D. A. Dickie and R. J. Gilliard Jr, *J. Am. Chem. Soc.*, 2023, **145**, 2028–2034.
41 P. Hindenberg, M. Busch, A. Paul, M. Bernhardt, P. Gemessy, F. Rominger and C. Romero-Nieto, *Angew. Chem., Int. Ed.*, 2018, **57**, 15157–15161.
42 A. Espineira-Gutierrez, I. Caro-Noakes, M. Zhang, M. Mas-Torrent, E. Regulska and C. Romero-Nieto, *Chem. Commun.*, 2025, **61**, 15590–15593.
43 R. Shankar, A. Jain, G. Kociok-Köhn, M. F. Mahon and K. C. Molloy, *Inorg. Chem.*, 2010, **49**, 4708–4715.
44 L. Britt and Y. Zhao, *Phys. Chem. Chem. Phys.*, 2024, **26**, 26526–26536.
45 F. Zettler, H. D. Hausen and H. Hess, *J. Organomet. Chem.*, 1974, **72**, 157–162.
46 (*a*) CCDC 2499454: Experimental Crystal Structure Determination, 2026, DOI: 10.5517/ccdc.csd.cc2pwwk1; (*b*) CCDC 2499455: Experimental Crystal Structure Determination, 2026, DOI: 10.5517/ccdc.csd.cc2pwwl2; (*c*) CCDC 2499456: Experimental Crystal Structure Determination, 2026, DOI: 10.5517/ccdc.csd.cc2pwwm3; (*d*) CCDC 2499457: Experimental Crystal Structure Determination, 2026, DOI: 10.5517/ccdc.csd.cc2pwwn4.